



Using unmanned aerial vehicle and volunteered geographic information to sophisticate urban flood modelling

Yuan-Fong Su¹, Yan-Ting Lin², Jiun-Huei Jang³, and Jen-Yu Han⁴

5 ¹ Slope and Hydrological Hazards Division, National Science and Technology Center for Disaster Reduction, New
Taipei City, 231, Taiwan

² Department of Civil Engineering, National Taiwan University, Taipei, 106, Taiwan

³ Department of Hydraulic and Ocean Engineering, National Cheng Kung University, Tainan, 701, Taiwan

⁴ Department of Civil Engineering, National Taiwan University, Taipei, 106, Taiwan

10 *Correspondence to:* Jiun-Huei Jang (jamesjang@mail.ncku.edu.tw)

Abstract.

Sophisticated flood simulation in urban areas is a challenging task due to the difficulties in data
acquisition and model verification. This study incorporates three rapid-growing technologies, i.e.
volunteered geographic information (VGI), unmanned aerial vehicle (UAV), and computational flood
15 simulation (CFS) to reconstruct the flash flood event occurred in 14 June 2015, GongGuan, Taipei. The
high-resolution digital elevation model (DEM) generated by a UAV and the real-time VGI photos
acquired from social network are served to establish and validate the CFS model, respectively. The DEM
data are resampled based on two grid sizes to evaluate the influence of terrain resolution on flood
simulations. The results show that flood scenario can be more accurately modelled as DEM resolution
20 increases with better agreement between simulation and observation in terms of flood occurrence time
and water depth. The incorporation of UAV and VGI lower the barrier of sophisticated CFS and shows
great potential in flood impact and loss assessment in urban areas.

Keywords: urban flooding; unmanned aerial vehicle; volunteered geographic information; computational
flood simulation; social media

25 1 Introduction

Flash flooding resulted from extreme heavy rainfall has been recognized as one of the most common
and destructive threats in recent years (Panthou et al., 2014; Chan et al., 2016; Bao et al., 2017; Busuioc



et al., 2017; Yang et al., 2017; Fu et al., 2019). Summarized in Table 1 are some of the flash flood events
in 2019 which have caused significant economic damages, life losses, and transportation interruption to
30 many major cities around the world. In the last two decades, computational flood simulation (CFS) has
been widely used to generate detailed flood scenarios in space and time by simulating water transportation
on surface and in sewer systems (Hunter et al., 2007; Kuiry et al., 2010; Seyoum et al., 2012; Jahanbazi
and Egger, 2014; Chang et al., 2015; Jang et al., 2018; Jang et al., 2019). However, these CFS models
require detailed DEM (digital elevation model) and real-time flood records for model construction and
35 validation, which are often inadequate in timeliness and accuracy for flash flood events occurring rapidly
in localized areas (Suarez et al., 2005; Yin et al., 2015; Pregolato et al., 2017).

Many researches have highlighted the influence of DEM resolution on hydrological modelling (Vaze
et al., 2009; Leitao et al., 2009; Li and Wong, 2010; Saksena and Marwade, 2015). For urban flood
modelling, Yang et al. (2014) recommended that the resolution of DEM should be higher than 5 m to
40 properly represent topographical indices. Flood simulation under coarser DEM resolutions tend to
overestimate the flood area and underestimate the flood depth in low-lying urban areas (Kim et al., 2020).
Recently, some authors mentioned that high resolution DEM has a greater influence on flood damage
estimation than on flood hazard estimation (Komolafe et al., 2018). Low spatial resolutions may generate
large errors in flood loss estimation due to improper representation of buildings (Afifi et al., 2009). Thus,
45 the acquisition of high resolution DEM has become a crucial task for sophisticated flood impact analysis
in urban areas.

Traditionally, the DEM data are derived by airborne Lidar which are too costly to be updated
frequently (Sankey et al., 2018), and flood records are usually obtained by post-disaster field
investigations that contain only rough coordinates and water depths without detailed time series. Recently,
50 two raising techniques namely unmanned aerial vehicle (UAV) and volunteered geographic information
(VGI) have been adopted for DEM generation and flood detection, respectively (Le Coz, et al., 2016;
Michelsen, et al., 2016; Starkey et al., 2017; Tauro et al., 2018). Studies have shown that digital elevation
models (DEM) derived by UAV have similar performances in urban overland flow modelling compared



with that derived from Lidar (Leitão et al., 2016). The VGI considers every citizen as a sensor to acquire
55 spatial data on a wide range of phenomena via crowdsourcing the keywords on social media such as
Facebook, Twitter, Instagram, etc. (Goodchild and Glennonm, 2010). Cervone et al. (2015) used Twitter
for remote sensing data collection and damage assessment of transportation infrastructure in the case
study of 2013 Boulder flood. Huang et al. (2018) proposed a convolutional neural network (CNN)
architecture to classify the flood pictures and a sensitivity test to extract flood-sensitive keywords that
60 were further used to refine the CNN results.

The applications of UAV and VGI open a new page for the sophistication of CFS models. Compared
with traditional methods, the UAV and VGI are more economical and applicable to retrieve detailed
terrain and flood information in real-time. The DEM generated by UAV can be served as the boundary
conditions to increase the spatial resolution of CFS and the time-series of water levels retrieved by VGI
65 can be used to validate the temporal variation of CFS results. With the help of UAV and VGI, this paper
introduces the methodologies and demonstrates the advantages of conducting high-resolution CFS for
flood analysis in urban areas, which are crucial for impact and loss assessment.

2 Materials and methods

The flash flood event occurred on 14 June 2015 in GongGuan, Taipei, Taiwan, is selected for case
70 study. The rainfall event occurred between 13:00-18:00 on 14 June 2015 with hourly rainfall peak of
131.5 mm/h during 14:30-15:30 as shown in Fig. 1. This rainfall intensity has exceeded the designed
drainage capacity of the sewer system and resulted in severe flash flooding in the cross-section of Keelung
Road and Changxing Street nearby the National Taiwan University. The study area and the location of the
rain gauge are shown in the Fig. 2. The DEM derived by UAV and the flood photos collected from VGI
75 are served to establish and validate the CFS, respectively. The conceptual flowchart of this study is shown
in Fig. 3. First, the UAV is deployed in a clear weather after the flood event to collect a great number of
images for generating DSM/DEM of the study area. Second, the rainfall and DEM under two different
resolutions are introduced into a CFS model to reconstruct the time series of flood depth and extent for
the selected flood event. Finally, the simulated results are compared with the VGI photos to see the



80 influence of DEM resolution on CFS.

2.1 DEM generated by UAV

The procedure of developing the urban 3D terrain is shown on the left side of Fig. 1. The methods of generating DEM from a set of aerial images or videos are quite mature (Pollefeys et al., 2008; Zhou et al., 2004), which are based on the fundamental principle of collinearity condition (Fig. 4) expressed by the

85 following equations:

$$x_p = -f \left[\frac{m_{11}(X_p - X_L) + m_{12}(Y_p - Y_L) + m_{13}(Z_p - Z_L)}{m_{31}(X_p - X_L) + m_{32}(Y_p - Y_L) + m_{33}(Z_p - Z_L)} \right] \quad (1)$$

$$y_p = -f \left[\frac{m_{21}(X_p - X_L) + m_{22}(Y_p - Y_L) + m_{23}(Z_p - Z_L)}{m_{31}(X_p - X_L) + m_{32}(Y_p - Y_L) + m_{33}(Z_p - Z_L)} \right] \quad (2)$$

where x_p and y_p are the image coordinate of any point p ; X_p, Y_p, Z_p represent the ground coordinate of point p ; X_L, Y_L, Z_L represent ground coordinate of the projection (optical) centre; f is the focal length; $m_{11} \dots m_{33}$ are the coefficients of a 3×3 rotation matrix defined by the angles ω , ϕ , and κ that transforms the ground coordinate system to the image coordinate system (Lillesand and Kiefer, 1999).

90 The six parameters X_L, Y_L, Z_L and ω , ϕ , and κ are used for exterior orientation of an image, which can be determined through the process of space resection as illustrated in Fig. 4. In the figure, the X , Y , and Z coordinate of any point in the matched stereopair of tilted images can be determined. Using a set of images taken by UAV, the ground coordinate of any point in the overlap of tilted images can be determined by the image matching method of structure-from-motion (Remondino and Fraser, 2006; Westoby et al.,
95 2012). Finally, the coordinate accuracies at check points are examined and the urban 3D terrain is obtained by resampling the coordinates to a regular grid system by the nearest neighbouring method.

The UAV used in this study is DJI Phantom 2 Vision+ (Da-Jiang Innovations) which weights 1.2 kg and has a camera with 4384×2466 pixels. The focal length of the camera is 3.3 mm and the field-of-view is 110 degrees. The UAV campaign was conducted in the early morning 22 July 2015 in cloudless
100 condition during 06:00 to 06:40 to reduce the disturbances from weather and traffic. In total, 589



positioned images were acquired with an overlap ratio of 75%–85% and a mean spatial resolution of 2.84 cm. After space intersection, the average ground sampling distance of point cloud is 0.03m. The UAV images were processed to generate orthomosaic image and digital surface model (DSM) with Pix4Dmapper Pro Version 1.4.46 (Pix4D). To derive absolute coordinates, three ground control points (GCPs) were distributed in the study area (Fig. 5). The coordinates of the three GCPs were acquired using the static positioning of Global Navigation Satellite System (GNSS) with positional accuracy in centimeter level. The absolute positions of the images, captured through the GNSS receiver in the UAV, were recorded to establish the coordinate system constrained on the three GCPs.

The lens distortion of the camera was calibrated by the flexible and powerful self-calibrating bundle adjustment (Remondino and Fraser, 2006). The calibration relies on the continuous overlapped-images so as to do the aerotriangulation adjustment. After the interior orientation and the coordinates of the object points are calculated, the correction Δx and Δy can be revised as below:

$$\begin{cases} \Delta x = -\Delta x_0 - \frac{x_i}{f} \Delta f + K_1 x_p r^2 + K_2 x_p r^4 + K_3 x_p r^6 + P_1 (r^2 + 2x_p^2) + 2P_2 x_p y_p \\ \Delta y = -\Delta y_0 - \frac{y_i}{f} \Delta f + K_1 y_p r^2 + K_2 y_p r^4 + K_3 y_p r^6 + P_2 (r^2 + 2y_p^2) + 2P_1 x_p y_p \end{cases} \quad (3)$$

where Δf is the principal distance error, Δx_0 and Δy_0 are the displacements of the principal point, K_1 , K_2 , and K_3 are the parameters of the radial distortion, P_1 and P_2 are the parameters of the decentering distortion, and r is the distance between the image point and the principal point. The calibrated parameters are listed in Table 2.

For CFS application, the DSM was converted to DEM by removing the vegetation and the viaduct. The vegetation such as shrubs and grasses is detected by the normalized difference vegetation index (NDVI) in the range of 0.2–0.3 (Candiago et al., 2015). Since the UAV images only observed red, green and blue bands, the near infrared band was built on a specific linear combination of the three bands with a lower-pass filter (Rabatel et al., 2011). To remove the viaduct, the elevation higher than the Keelung Road (9 m) was selected as a threshold value to identify the viaduct positions. Based on the NDVI and



elevation thresholds, the vegetation and viaducts were filtered out in DEM so that flood water can transport smoothly on ground surface. However, unlike traditional DEM, the elevations of buildings were
125 not removed to prevent the transverse of runoff water.

2.2 VGI from social media

Ethical and legal concerns are big issues for collecting and using VGI (Foody et al., 2017). Fortunately, the Copyright Act and Relative Laws in Taiwan allows researchers to quote, within a reasonable scope, publicly released works for reports, comment, teaching, research or other legitimate purposes (Copyright
130 Act and Relative Laws, 2016). Based upon the Act, the VGI data used in this study are collected from the most famous Bulletin Board System (BBS) in Taiwan named PTT. There are 8 photos collected from PTT posted during 15:20~16:30 on 14 June 2015. From these photos, we visually identified 8 locations in the study area as shown in Fig. 6. The timestamp and the virtual water depths in these photos are served to validate the CFS model. Although the timestamp when photos were posted on internet may not always be
135 the acquisition time and the flood depth estimated from photos may be subject to experts' experience, these uncertainties can be reduced by the functions of "live stream" and "image recognition" on social media

2.3 CFS model

The CFS model used in this study was developed by Jang et al. (2018), in which a 2D Overland Flow
140 Model (OFM) is coupled with a 1D Sewer Flow Model (SFM) for sophisticated flood simulation in cities with drainage systems. The OFM and SFM are established based on shallow water equations and finite difference numerical methods. The alternate direction explicit scheme and implicit backward Euler algorithm are used to solve the OFM and SFM, respectively. The SFM adopted Preissmann slot method (Cunge and Wegner, 1964) to calculate the full and partially-full flow conditions at the same time. For
145 the OFM simulation, the elevation at each grid center is extracted from the DEM data. When rain drops, the OFM is firstly initiated for surface water routing and the SFM is then initiated by the water that flows into the sewer pipes via street inlets. When the sewer pipes get full, the sewer water surcharges back onto



ground surface via manholes. In the simulation process, the water exchanged between the two models are determined by weir and orifice functions via one-to-one relationship. The details of the CFS model can be referred to Jang et al. (2018; 2019).

3 Results and discussions

3.1 DEM

The DEM accuracy are examined at the three GCPs. The errors in X , Y and Z directions range from -0.006 to 0.025 m, -0.038 to 0.061 m, and -0.016 to 0.002 m, respectively. The root mean square errors of the absolute coordinate at the three GCPs are less than 0.046m (Table 3). The orthoimage and the DEM resampled under spatial resolutions of 0.5 m and 5 m are shown in Fig. 7. In the figure, the elevation distributes from 5.5 to 55.8 m and the buildings are displayed in the warm colors.

3.2 Flood extent

To discover the influence of DEM resolution on flood simulation, the grid meshes of the CFS model are established under a fine grid size (0.5 m \times 0.5 m) and a coarse grid size (5 m \times 5 m), respectively, in which the elevation at each grid center is extracted from the DEM with accordant resolution. The flood extents simulated under the two DEM resolutions at different time are displayed in Fig. 8, in which the VGI points out of the 8 locations are marked if the simulated flood depths exceed 0.05 m. The value of 0.05 m is selected as the threshold because above which road traffic will be affected. In the case with 0.5 m DEM resolution, flooding starts around 14:00 at points #4, #7, and #8, peaks around 15:00 at all points, and retreats at 17:00 back to original points. In comparison, flooding simulated under 5 m DEM resolution occurs earlier and retreats much later with some water trapped between buildings. Observing the flood maps between 15:00-18:00, the water inundated on the rooftops of buildings can be properly simulated in the case with fine DEM resolution but not in the case with coarse resolution.

3.3 Flood volume

The time series of flood volume simulated under the two DEM resolutions are displayed in Fig. 9.



Compared with the case with 0.5 m DEM resolution, the flood volume simulated under 5 m DEM resolution arises faster but descends slower with a higher and earlier appearance of flood peak. This implies that, when DEM resolution decreases, the topography becomes rugged, the friction increases, and the flood water travels slower. Table 4 compares the simulation and observation results in terms of flood occurrence time and water depth. The timestamps and estimated water depths (WD) are obtained from the VGI photos in Fig. 6, and the flood durations at the eight VGI points when the water depth exceeds 0.05 m are determined based on the CFS results. It is seen that the timestamps of VGI photos all lie within the simulated flood duration at the points with observed WD larger than 0.05 m (points #1, #2, #4, #7, and #8). At the rest points, the simulated and observed WDs are both smaller than 0.5 m. This good agreement between observation and simulation reveals that the flood model is accurate in rebuilding the process of flood transport under both DEM resolutions.

Compared with the flood durations simulated under 0.5 m DEM resolution, those under 5 m DEM resolution increase by 30 to 200 minutes at points #1, #2 and #3. This indicates a chance that the flood durations are overestimated under 5 m DEM resolution because no further VGI photos were posted after 15:40 at point #2. The flood impact on traffic could be overestimated if low-resolution DEM data are used for flood simulation. The spatial resolution of DEM in urban areas should be at least finer than road width so that road profiles can be clearly displayed; otherwise, runoff transportation around buildings and on roads cannot be correctly simulated. Sub-meter resolution DEM data generated by UAV are adequate for assessing the impact of localized flooding on transportation in cities. Some open accessible topographic datasets, such as the 30 m resolution DEM by STRM from NASA (<https://www2.jpl.nasa.gov/srtm/>) and the open DEM in Taiwan with 20 m resolution (<https://data.gov.tw/dataset/35430>) are too coarse to serve the purpose.

3.4 Simulation efficiency

Flood simulation under high grid resolutions is usually more time-consuming than that that under coarse grid resolutions due to the increase in grid numbers. The choice of grid resolution for flood simulation is a tradeoff between accuracy and efficiency. For the study area in this research, there are



573,000 and 5,730 grids for the mesh with grid size 0.5 m and the mesh with grid size 5 m, which consumes 1,127 mins and 16 mins of computational time, respectively (with Intel Core i7-7700K CPU @ 4.2GHz and 64 GB RAM). For disaster emergency response in regional scale, flood simulation under coarse grid resolution is enough to gain a fast and overall understanding of flood pattern. However, for evaluating flood impact on critical infrastructures such as metro stations, power facilities, schools, government agencies, hospitals, etc., high-resolution flood simulation is required.

4 Conclusions

Flash flood analysis by CFS in urban area is a challenging task since it requires high-resolution terrain and real-time flood information for model construction and validation. Aided by the rapid growing technologies of remote sensing and crowdsourcing, it is possible to update DEM data and record the flood depth in real time by UAV and VGI. In this study, we adopt the UAV and VGI to sophisticate CFS modeling in the reconstruction of a flash flood event occurred on 14 June, 2015, Taipei City. The CFS model is routed under two DEM resolutions with grid size 0.5 m and 5 m, separately. In the case with finer DEM, the simulation results are in better agreement with the observation in terms of flood extent, depth, and occurrence. Using DEM with coarse resolution for CFS overestimates the flood duration on roads which may provide bias information to decision makers for impact assessment on traffic and economic losses. Compared with traditional methods, the UAV and VGI are more economical and applicable in acquiring necessary data for high-resolution CFS.

Data availability. DEM and VGI data used in this study are available by contacting the authors.

Author contributions.

JHJ and YFS conceived the idea; YTL and JHJ conducted the experiments and analyses; YFS, JHJ, and YTL wrote the article; JYH provided comments.

Competing interests. The authors declare that they have no conflict of interest.



225 *Acknowledgements.* This work was supported by the Ministry of Science and Technology [MOST 108-2625-M-006-008].

References

230 Bao, J., Sherwood, S.C., Alexander, L.V., and Evans, J.P.: Future increases in extreme precipitation exceed observed scaling rates. *Nat. Clim. Change*, 7, 128–132, <http://dx.doi.org/10.1038/nclimate3201>, 2017.

Busuioc, A., Baciu, M., Breza, T., Dumitrescu, A., Stoica, C., and Baghina, N.: Changes in intensity of high temporal resolution precipitation extremes in Romania: implications for Clausius-Clapeyron scaling, *Clim. Res.*, 72, 239–249, 235 <https://ui.adsabs.harvard.edu/#abs/2016EGUGA..1814561B/abstract>, 2017.

Candiago, S., Remondino, F., De Giglio, M., Dubbini, M., and Gattelli, M.: Evaluating multispectral images and vegetation indices for precision farming applications from UAV images, *Remote Sens.*, 7(4), 4026–4047, <https://doi.org/10.3390/rs70404026>, 2015.

240 Cervone, G., Sava, E., Huang, Q., Schnebele, E., Harrison, J., and Waters, N.: Using Twitter for tasking remote-sensing data collection and damage assessment: 2013 Boulder flood case study, *Int. J. Remote. Sens.*, 37(1), 100–124, <https://doi.org/10.1080/01431161.2015.1117684>, 2015.

Chan, S.C., Kendon, E.J., Roberts, N.M., Fowler, H.J., and Blenkinsop, S.: The characteristics of summer sub-hourly rainfall over the southern UK in a high-resolution convective permitting model. *Environ. Res. Lett.*, 11, 094024. <http://dx.doi.org/10.1088/1748-9326/11/9/094024>, 2016.

245 Chang, T.J., Wang, C.H., and Chen, A.S.: A novel approach to model dynamic flow interactions between storm sewer system and overland surface for different land covers in urban areas, *J. Hydrol.* 524, 662–679, <https://doi.org/10.1016/j.jhydrol.2015.03.014>, 2015.

Copyright Act 2016, Intellectual Property Office, Ministry of Economic Affairs, ROC., rom: <https://www.tipo.gov.tw/public/Attachment/71417531682.pdf>, last access: 26 September, 2019.

250 Cunge, J.A. and Wegner, M.: Intégration numérique des équations d'écoulement de barré de Saint-Venant



- par un schéma implicite de différences finies, *La Houille Blanche*, 1, 33-39,
<https://doi.org/10.1051/lhb/1964002>, 1964.
- Floodlist, <http://floodlist.com/>, last access: 16 Jan, 2020.
- Footy, G., See, L., Fritz, S., Mooney, P., Olteanu-Raimond, A-M., Fonte, C.C., and Antoniou, V.:
255 Mapping and the Citizen Sensor. London: Ubiquity Press, DOI: <https://doi.org/10.5334/bbf>. License:
CC-BY 4.0., 2017.
- Fu, J.C., Huang, H.Y., Jang, J.H., and Huang, P.H.: River stage forecasting using multiple additive
regression trees, *Water Res. Manag.* 33, 4491–4507, <https://doi.org/10.1007/s11269-019-02357-x>,
2019.
- 260 Goodchild, M. F. and Glennon, J. A.: Crowdsourcing geographic information for disaster response: A
research frontier, *Int. J. Digit. Earth*, 3, 231–241, <https://doi.org/10.1080/17538941003759255>, 2010.
- Huang, X., Wang, C., Li, Z., and Ning, H.: A visual-textual fused approach to automated tagging of flood-
related tweets during a flood event, *Int. J. Digit. Earth*, 1248–1264,
<https://doi.org/10.1080/17538947.2018.1523956>, 2018.
- 265 Hunter, N.M., Bates, P.D., Horritt, M.S., and Wilson, M.D.: Simple spatially-distributed models for
predicting flood inundation: A review, *Geomorphology* 90(3–4), 208–225,
<https://doi.org/10.1016/j.geomorph.2006.10.021>, 2007.
- Jahanbazi, M. and Egger, U.: Application and comparison of two different dual drainage models to assess
urban flooding. *Urban Water J.*, 11, 584–595, <https://doi.org/10.1080/1573062X.2013.871041>, 2014.
- 270 Jang, J.H., Chang, T.H., and Chen., W.B.: Effect of inlet modelling on surface drainage in coupled urban
flood simulation. *J. Hydrol.*, 562: 168–180., <https://doi.org/10.1016/j.jhydrol.2018.05.010>, 2018.
- Jang, J.H., Hsieh C.T., and Chang, T.H.: The importance of gully flow modelling to urban flood simulation,
Urban Water J., 16(5): 377-388, <https://doi.org/10.1080/1573062X.2019.1669198>, 2019.
- Kim, Y.D., Tak, Y.H., Park, M.H., Kang, B.: Improvement of urban flood damage estimation using a high-
275 resolution digital terrain. *J. Flood Risk Manag.*; 13 (Suppl. 1):e12575,
<https://doi.org/10.1111/jfr3.12575>, 2020
- Komolafe, A., Herath, S. and Avtar, R.: Sensitivity of flood damage estimation to spatial resolution. *J.*



- Flood Risk Manag., 11: S370-S381, <https://doi.org/10.1111/jfr3.12224>, 2018
- Kuiry, S. N., Sen, D., and Bates, P. D.: A coupled 1D-quasi 2D flood inundation model with unstructured
280 grids, *J. Hydraul. Eng.* 136, 493–506, [https://doi.org/10.1061/\(ASCE\)HY.1943-7900.0000211](https://doi.org/10.1061/(ASCE)HY.1943-7900.0000211), 2010.
- Le Coz, J., Patalano, A., Collins, D., Guillén, N.F., García, C.M., Smart, G.M., Bind, J., Chiaverini, A.,
Le Boursicaud, R., and Dramais, G.: Crowdsourced data for flood hydrology: Feedback from recent
citizen science projects in Argentina, France and New Zealand. *J. Hydrol.*, 541, 766-777,
<https://doi.org/10.1016/j.jhydrol.2016.07.036>, 2016.
- 285 Leitão, J.P. and Boonya-aroonnet, S. and Prodanović, D. and Maksimović, Č.: The influence of digital
elevation model resolution on overland flow networks for modelling urban pluvial flooding. *Water
Sci Technol*; 60 (12): 3137–3149, <https://doi.org/10.2166/wst.2009.754>, 2009
- Leitão, J.P., Vitry, M.M.d., Scheidegger, A., and Rieckermann, J.: Assessing the quality of digital elevation
models obtained from mini unmanned aerial vehicles for overland flow modelling in urban areas,
290 *Hydrol. Earth Syst. Sci.*, 20, 1637–1653, <https://doi.org/10.5194/hess-20-1637-2016>, 2016.
- Li, J., and Wong, D.: Effect of DEM sources on hydrologic applications. *Comput. Environ. Urban*, 34,
251-261, <https://doi.org/10.1016/j.compenvurbsys.2009.11.002>, 2010.
- Lillesand, T.M. and Kiefer, R.W. (4th Ed.): *Remote Sensing and Image Interpretation*, New York, Wiley.,
1999.
- 295 Michelsen, N., Dirks, H., Schulz, S., Kempe, S., Al-Saud, M., and Schüth, C.: Youtube as a crowd-
generated water level archive, *Sci. Total Environ.*, 568, 189-195,
<https://doi.org/10.1016/j.scitotenv.2016.05.211>, 2016.
- Panthou, G., Vischel, T., and Lebel, T.: Recent trends in the regime of extreme rainfall in the Central Sahel.
Int. J. Climatol., 34, 3998-4006., <https://doi.org/10.1002/joc.3984>, 2014.
- 300 Pollefeys, M., Nister, D., Frahm, J.-M., Akbarzadeh, A., Mordohai, P., Clipp, B., Engels, C.: Detailed
real-time urban 3D reconstruction from Video. *Int. J. Comput. Vision*, 78, 143-167,
<https://doi.org/10.1007/s11263-007-0086-4>, 2008.
- Pregolato, M., Ford, A., Wilkinson, S.M., and Dawson, R.J.: The impact of flooding on road transport:
A depth-disruption function. *Transpor. Res. D-TR E.*, 55, 67-81,



- 305 <https://doi.org/10.1016/j.trd.2017.06.020>, 2017.
- Rabatel, G., Gorretta, N., and Labbé S.: Getting NDVI Spectral Bands from a Single Standard RGB Digital Camera: A Methodological Approach. In: Lozano J.A., Gámez J.A., Moreno J.A. (Eds.): Advances in Artificial Intelligence. CAEPIA 2011. Lecture Notes in Computer Science (pp. 333-342), vol. 7023. Springer, Berlin, Heidelberg: La Laguna, Spain, 2011.
- 310 Remondino, F., and Fraser, C.: Digital camera calibration methods: considerations and comparisons. International Archives of Photogrammetry, Remote Sensing and Spatial Information Sciences, 36, 266-272, <http://citeseerx.ist.psu.edu/viewdoc/download?doi=10.1.1.67.8805&rep=rep1&type=pdf>, 2006.
- Saksena, S., and Merwade, V.: Incorporating the effect of DEM resolution and accuracy for improved flood inundation mapping. J. Hydrol., 530, 180–194, <https://doi.org/10.1016/j.jhydrol.2015.09.069>, 2015.
- Sankey, T.T., McVay, J., Swetnam, T.L., McClaran M.P., Heilman, P., Nichols, M.: UAV hyperspectral and lidar data and their fusion for arid and semi-arid land vegetation monitoring, Remote Sen. Eco. Conserv., 4:20–33, 2018.
- 320 Starkey, E., Parkin, G., Birkinshaw, S., Large, A., Quinn, P., and Gibson, C.: Demonstrating the value of community-based ('citizen science') observations for catchment modelling and characterization, J. Hydrol., 548, 801-817, <https://doi.org/10.1016/j.jhydrol.2017.03.019>, 2017.
- Suarez, P., Anderson, W., Mahal, V., and Lakshmanan, T.R.: Impacts of flooding and climate change on urban transportation: A systemwide performance assessment of the Boston Metro Area. Transpor. Res. D-TR E., 10, 231-244, <https://doi.org/10.1016/j.trd.2005.04.007>, 2005.
- 325 Seyoum, S.D., Vojinovic, Z., Price, R.K., and Weesakul, S.: Coupled 1D and Noninertia 2D flood inundation model for simulation of urban flooding. J. Hydraul. Eng. 138, 23–34, [https://doi.org/10.1061/\(ASCE\)HY.1943-7900.0000485](https://doi.org/10.1061/(ASCE)HY.1943-7900.0000485), 2012
- Tauro, F., Selker, J., van de Giesen, N., Abrate, T., Uijlenhoet, R., Porfiri, M., Manfreda, S., Caylor, K., 330 Moramarco, T., and Benveniste, J.: Measurements and observations in the XXI century (MOXXI): innovation and multi-disciplinarity to sense the hydrological cycle. Hydrolog. Sci. J., 63, 169–196,



<https://doi.org/10.1080/02626667.2017.1420191>, 2018.

Vaze, J., Teng, J., and Spencer, G.: Impact of DEM accuracy and resolution on topo-graphic indices.

Environ. Model. Softw. 25, 1086–1098, <https://doi.org/10.1080/014311600209931>, 2010.

335 Westoby, M.J., Brasington, J., Glasser, N.F., Hambrey, M.J., and Reynolds, J.M.: Structure-from-Motion photogrammetry: A low-cost, effective tool for geoscience applications. *Geomorphology*, 179, 300–314, <https://doi.org/10.1016/j.geomorph.2012.08.021>, 2012.

Yang, P., Ames, D. P., Fonseca, A., Anderson, D., Shrestha, R., Glenn, N. F., and Cao, Y.: What is the effect of LiDAR derived DEM resolution on large-scale watershed model results? *Environ. Model.*

340 *Softw.*, 58, 48–57, <https://doi.org/10.1016/j.envsoft.2014.04.005>, 2014.

Yang, P., Ren, G., and Yan, P.: Evidence for a strong association of short-duration intense rainfall with urbanization in the Beijing urban area. *J. Clim.*, 5851–5870, <https://doi.org/10.1175/JCLI-D-16-0671.1>, 2017.

Yin, J., Yu, D., Yin, Z., Liu, M., and He, Q.: Evaluating the impact of risk of pluvial flash flood in intra-

345 urban road network: A case study in the city center of Shanghai, China. *J. Hydro.*, 537, 138–145, <https://doi.org/10.1016/j.jhydrol.2016.03.037>, 2016.

Zhou, G., Song, C., Simmers, J., and Cheng, P.: Urban 3D GIS from LiDAR and digital aerial images.

Computer Geosciences, 30, 345–353, <https://doi.org/10.1016/j.cageo.2003.08.012>, 2004.



Table 1: Major flash flood events around the world in 2019 (Floodlist, 2019).

Location and Date	Description
Tafalla, Spain 08, July	A rainfall record of 100.2 mm in 24 hours with highest hourly rainfall of 63.8 mm is observed in Tafalla, Spain. Rail transportation and major roads such as N-121 and AP-15 are interrupted.
Washington, USA 08, July	About 127mm rainfall downpoured in 24 hours in Frederick, nearby Washington D.C. and the Reagan National Airport in Washington D.C. reported 83.82mm of rain in 1 hour on 08 July. Around 20 roads in the D. C. area were closed and several Amtrak trains were stopped due to flooded tracks near Alexandria, Virginia.
Texas, USA 24, June	More than 317.5 mm of rain pounded Harlingen, Cameron, Texas, USA within 4 hours. Several streets were flooded and blocked.
Recife, Brazil 13, June	The city recorded 117mm of rain within 6 hours and it is roughly one-third of the monthly average of June.
London, England 11, June	The area nearby London received 1~2 months worth of rain in 24 hours. Heavy rain has caused widespread disruption in England, including flooded roads, railways, and a hospital.
Hesse, Germany 21, May	In Hesse and North Rhine-Westphalia up to 50 mm of rain fell in 6 hours causing flooding of roads and car accident.
Hsinchu, Taiwan 17, May	A rainfall record of 341mm observed in 6 hours with highest hourly rainfall of 91.5 mm. Some major roads in Hsinchu county were blocked due to flooding.
Yonaguni, Japan 13, May	The highest rainfall record of 367 mm in 6 hours in 50 years was recorded in Yonaguni, Okinawa. Airport was temporarily closed and transportation was interrupted.
Texas and Kansas, USA 07, May	A record of 177.8mm of rain in 4 hours observed in Texas and 127mm of rain in 2 hours observed in Kansas. Major roadways were impassable.
Abijan, Ghana 08, April	A record of 53mm of rain in 24 hours observed on Abijan and several areas of the city were flooded, including Abosseyyokai, Awudome, Kwame Nkrumah Interchange, Kaneshie, Ashaiman, and Alajo. Scores of vehicles were trapped in the water.
Lorestan, Iran 31, March	In a 24 hours period from 31 March, 2019, Khorramabad, capital of Lorestan Province recorded 106.9mm of rain and Hamedan in Hamadan Province, recorded 98.6mm. The flooding has caused damage to bridges, roads, infrastructure and homes in Lorestan province.
Shiraz, Iran 25, March	A major flash flooding hit the city of Shiraz after 18mm of rain fell in 10min. Major roadways were flooded and over 150 vehicles dragged by the powerful flood waters.
San Paulo, Brazil 10, March	Nearly 110mm of rain, 70% of the month worth of March, fell within 24 hours and the flooding water tossed cars atop buildings and into trees.
Daintree, New Zealand 28, January	The Daintree River village of Whyanbeel Valley measured a record 472mm in 24 hours which worth a month of rainfall in Jan. Major roadways and Ferry were closed due to flooding.
Beira, Mozambique 22, January	About 277mm of rain was reported in Beira in the 24 hours, more than 250mm expected in the entire month of January, due to Cyclone Desmond. Major roadways were flooded and scores of cars were submerged.
Chaco, Argentina 08, January	Resistencia, Chaco recorded 224 mm of rain within 24 hours while 180mm of rain fell in just 80 minutes. Major roadways were flooded.



Table 2: Calibrated parameters for camera on the UAV.

Parameters		Value	Parameters		Value
Image size (pix)		4384*2466	Focal length(mm)		3.32347
Pixel size (μm)		1.3306	Radial distortion	K_1	-0.382174
Principal point (mm)	x_0	2.9718		K_2	0.182175
	y_0	1.71489		K_3	-0.046338
CCD size (mm)	Width	5.83335	Decentering distortion	P_1	0.000508
	Height	3.28126		P_2	0.000017

Table 3: Accuracy of the ground control points (m).

	GCP_1	GCP_2	GCP_3	Mean	Std.	RMSE
Error X	-0.006	0.025	-0.019	0.000	0.018	0.018
Error Y	0.061	-0.035	-0.038	-0.004	0.046	0.046
Error Z	0.002	-0.016	0.000	-0.005	0.008	0.009

Table 4: Comparison between CFS and VGI results.

Point (#)	Latitude (degree)	Longitude (degree)	Observation (VGI)		Flood duration with $WD \geq 0.05$ m (CFS)	
			Timestamp	WD (m)	DEM 0.5 m	DEM 5 m
1	121.544603	25.016963	15:20	≥ 0.05	14:40–15:30	14:00–15:50
2	121.543563	25.016420	15:40	≥ 0.05	15:00–15:50	13:50–18:00
3	121.544612	25.017167	16:10	< 0.05	15:00–15:30	14:40–15:40
4	121.544236	25.017421	16:10	≥ 0.05	14:00–18:00	13:50–18:00
5	121.543351	25.017728	16:20	< 0.05	14:40–16:10	14:40–16:00
6	121.543462	25.017716	16:20	< 0.05	14:40–15:40	14:40–15:40
7	121.543674	25.017670	16:30	≥ 0.05	14:00–17:50	14:00–18:00
8	121.543476	25.016745	16:30	≥ 0.05	14:00–18:00	13:50–18:00

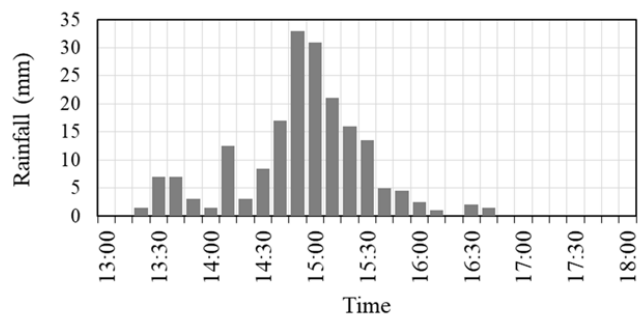


Figure 1: The rainfall hyetograph on 14 June 2015 at GongGuan rain-gauge station (C1A760).

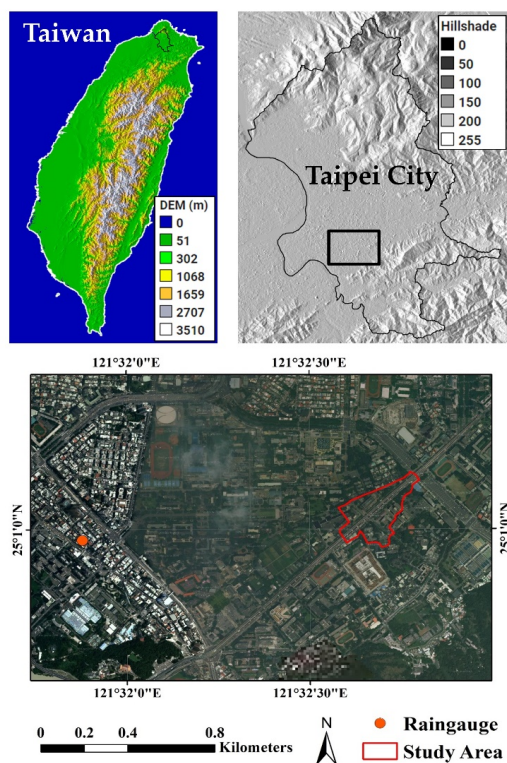


Figure 2: Study area (red polygon) at GongGuan, Taipei, Taiwan (the Google Earth images sourced from © Google, Landsat/Copernicus and the shading image was derived from SRTM with 30 meter resolution).

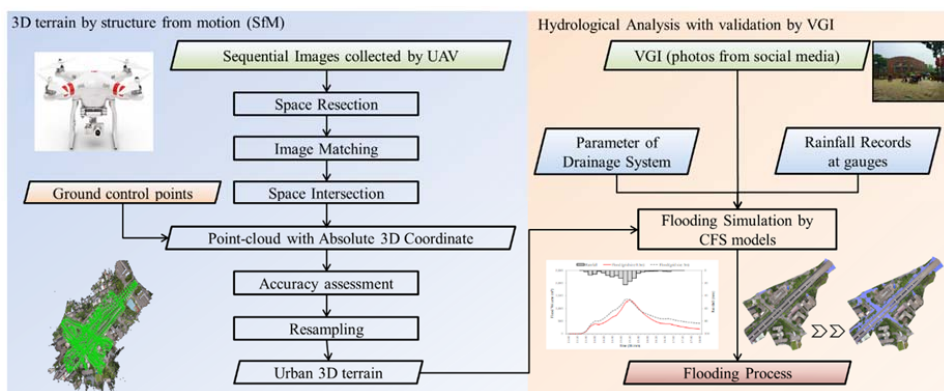


Figure 3: Conceptual flowchart of this study (the VGI photo was adopted from PTT, Taiwan).

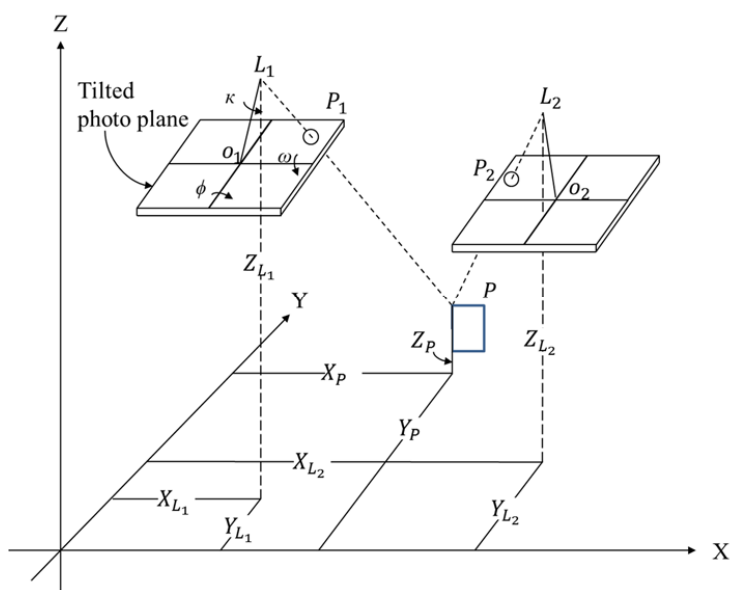


Figure 4: Illustration of collinearity condition and space intersection (adapted from Lillesand and Kiefer, 1999).

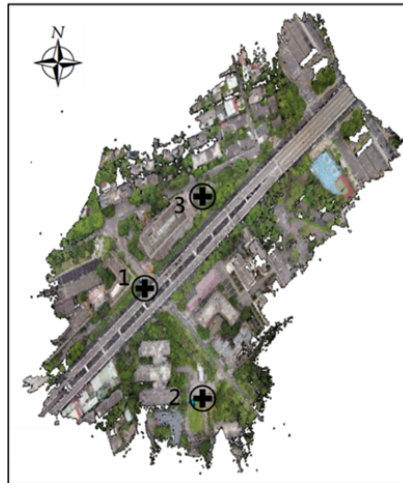


Figure 5: Images taken by UAV and the distribution of the ground control points.



Figure 6: VGI photos from social media and their acquisition time (adopted from PTT, Taiwan).

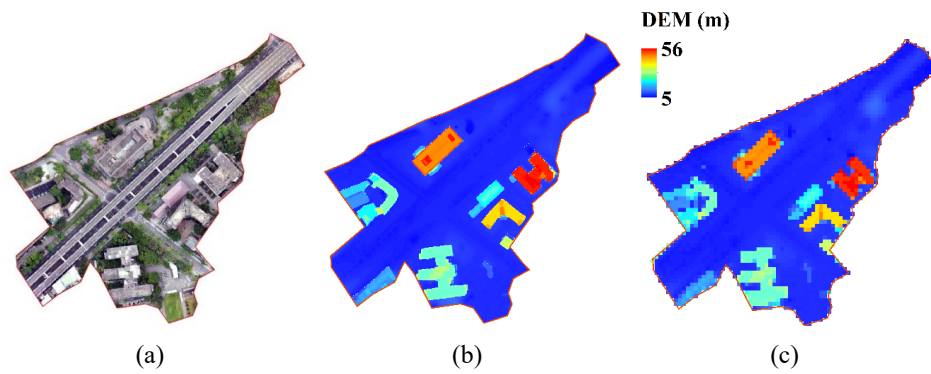
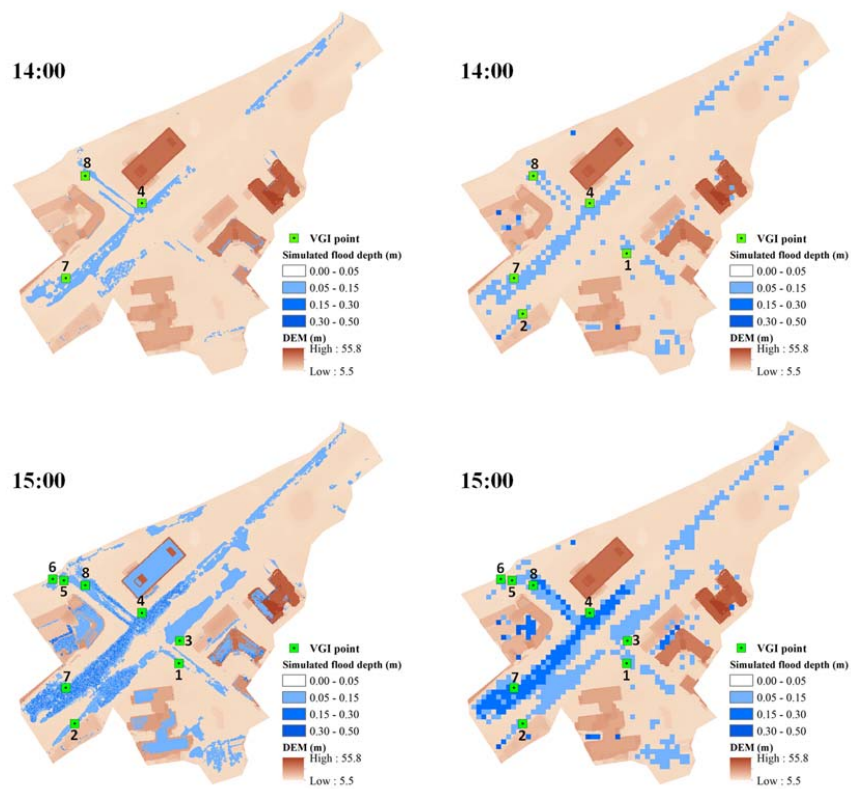


Figure 7: (a) Orthoimage; (b) the DEM with spatial resolution of 0.5 m; (c) the DEM with spatial resolution of 5 m



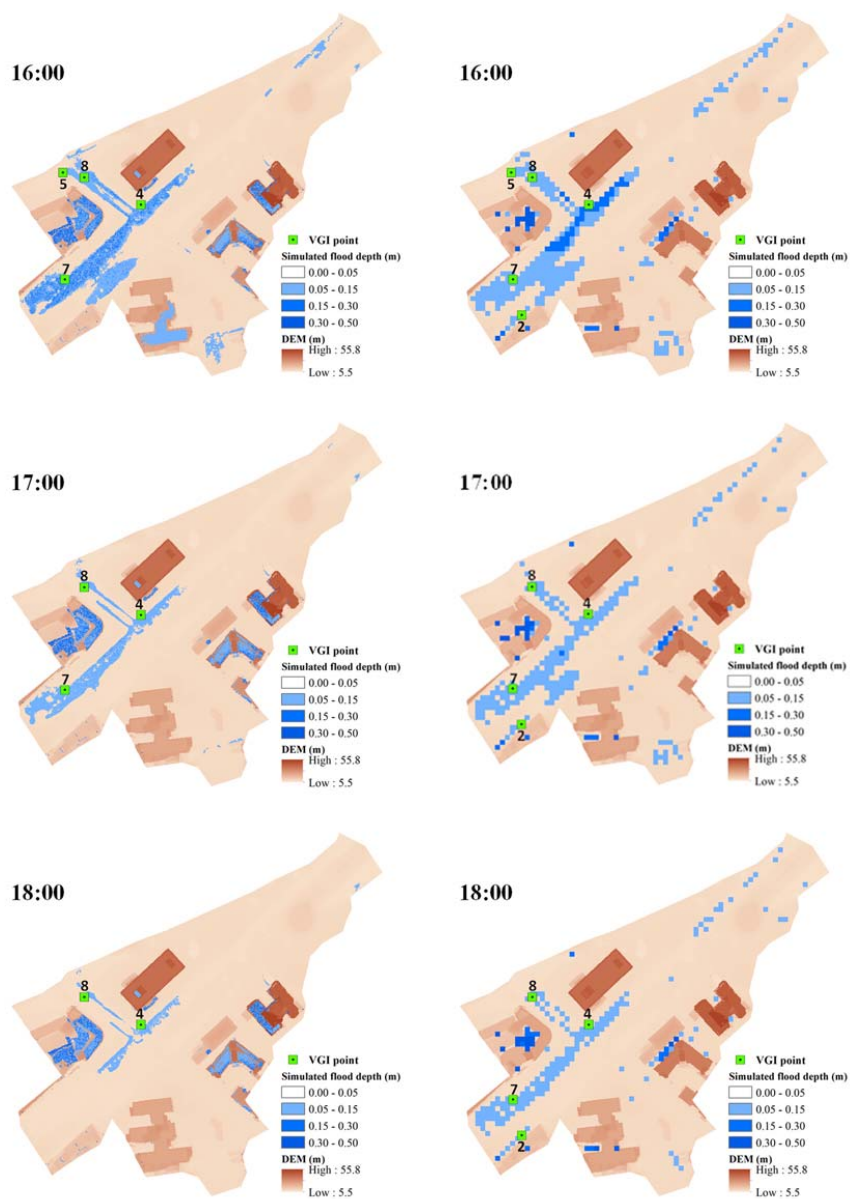


Figure 8: Simulated flood extents at different time under DEM resolution 0.5 m (left) and DEM resolution 5 m (right).

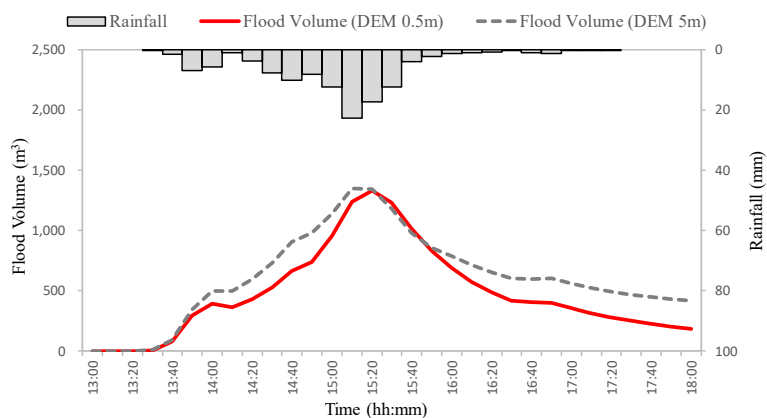


Figure 9: Comparison of simulated flood volume under two DEM resolutions.